IEEE Access
Multidisciplinary ⋮ Rapid Review ⋮ Open Access Journal

Received 18 November 2024, accepted 7 December 2024, date of publication 11 December 2024,
date of current version 31 December 2024.

*Digital Object Identifier 10.1109/ACCESS.2024.3514867*

RESEARCH ARTICLE

# Active Disturbance Rejection Power Predictive Control of Rectifier Based on Bus Voltage Optimized ESO Observer

**XIONG XIAO[1], JUNYU ZHAO[1], XIAN SONG[2], YUNTAO ZHAO[3], YONGJUN ZHANG[1], AND FEI ZHANG[1], (Member, IEEE)**

[1]Institute of Engineering Technology, University of Science and Technology Beijing, Beijing 100083, China
[2]Department of Applied Biology and Chemical Technology, The Hong Kong Polytechnic University, Hong Kong, China
[3]School of Information Science and Engineering, Wuhan University of Science and Technology, Wuhan 430081, China

Corresponding author: Yongjun Zhang (zhangyj@ustb.edu.cn)

This work was supported in part by the Key Research and Development Program of Guangxi under Grant AB21196025; and in part by the Engineering Research Center for Metallurgical Automation and Measurement Technology of Ministry of Education, Wuhan University of Science and Technology, under Grant MADTOF2023A02.

**ABSTRACT** In the control system of three-phase voltage source pulse width modulation rectifier, dynamic control of direct current bus voltage has become the research focus. This paper proposes an active disturbance rejection control- model predictive direct power control strategy, without a bus voltage sensor, aiming at improving the fault tolerance of the direct current side. This strategy considers the dynamic response ability of rectifier operation without a voltage sensor and avoids the outer loop feedback distortion caused by voltage sensor faults. Model predictive direct power control is used in the inner loop. For the improvement of system response performance, bus voltage extended state observer and active disturbance rejection controller are designed for the outer loop. In addition, error differential term is added to the extended state observer to realize fast tracking of dynamic voltage without sensor. An adaptive threshold is designed by comparing the residual error and threshold, which realizes the fast switching and system normal operation under voltage sensor fault. The proposed control strategy is verified by simulation and experiment. The results show that the observation error of the proposed strategy is within 2 V, which is down about 2 V from direct power control and model predictive direct power control. When the bus voltage step, the observed voltage fluctuation is 5 V, and the adjustment time is about 75 ms. Combined with the strategy, extended state observer can well track the dynamic change of bus voltage and realizes automatic switching control under sensor fault.

**INDEX TERMS** Adaptive threshold, bus voltage sensorless, extended state observer, pulse width modulation rectifier.

## ACRONYMS

| | |
|---|---|
| PWM | Pulse width modulation. |
| MPC | Model predictive control. |
| ESO | Extended state observer. |
| PMSM | Permanent magnet synchronous motor. |
| SMPIC | Sliding mode PI control. |
| APF | Active power filter. |
| ADRC | Active disturbance rejection control. |
| MPDPC | Model predictive direct power control. |
| MPDTC | Model predictive direct torque control. |

The associate editor coordinating the review of this manuscript and approving it for publication was Alfeu J. Sguarezi Filho.

## I. INTRODUCTION

Three-phase voltage-type pulse width modulation (PWM) rectifier is an efficient, eco-friendly, and reliable power electronic conversion device. It has many advantages such as high energy density, bidirectional flow, and adjustable power factor [1], [2], and has been widely used in many fields such as industrial drives, new energy generation, and uninterruptible power supplies [3], [4]. As the key link connecting the rectification and inversion sides, the direct current (DC) bus is crucial for the stable operation of the rectifier. However, due to the harsh industrial production environment, voltage sensor signals are vulnerable to faults such as temperature drift, zero offset, gain changes, and signal loss due to factors

such as temperature, humidity, electromagnetic interference, and mechanical vibration. This can cause deviations in the voltage feedback value and affect the control effect of the system. Therefore, operating the system without a voltage sensor under faulty conditions has received widespread attention from scholars [6].

The DC bus voltage sensorless control is an important technique in the field of power electronics. Based on state observer, model predictive control (MPC) and adaptive control, this strategy can be used to regulate and stabilize the DC bus voltage, which frees the motor from dependence on voltage sensors and reduces the hardware cost of the system. However, some research challenges remain to be addressed: 1) The control system must be able to respond to changes in load in real time. 2) The algorithm should have an excellent robustness for parameter changes and external disturbance. 3) The nonlinear characteristics of motors require complex control algorithms.

Among the research on the DC bus voltage sensorless control, the most widely used method is based on voltage observers. When the sensor fails, the observer estimation can directly replace the sensor measurement, which can simultaneously achieve diagnosis of sensor faults and fault-tolerant control. Reference [7] proposed the idea of combining bus voltage observer with model error rolling optimization and designed a MPC method without bus voltage sensor. Reference [8] constructed an adaptive voltage observer, which consists of an adaptive neural network identifier and an adaptive neural network filter, and achieved power prediction control of PWM rectifiers without a grid-side voltage sensor. Reference [9] proposed a nonlinear damping output-feedback voltage control for DC/DC converters via model-Independent voltage derivative observer, which reduces the static estimation error by the structure observer gain in the absence of system information. Reference [10] introduced a control technology for a single-phase rectifier under the distorted grid condition without an AC voltage sensor. However, above researches focused on improving the static observation accuracy, but paid less attention to improve the dynamic observation accuracy. Combining the observer with appropriate control methods can effectively solve the above problem.

Compared with commonly used observers, the Extended State Observer (ESO) operation process is not complicated and there are no restrictions on its applicable range and constraints [11]. Currently, it can achieve static and dynamic estimation of variables accurately and has been widely used in the field of motor control. Reference [12] proposed a new ESO design technique which is based on cascading a series of first-order ESOs. Benefited from the cascade design, saturations can be inserted into the observer internal variables to limit the maximal implemented gain. Reference [13] designed a robust voltage controller based on resonant ESO(RESO). The resonant unit was embedded into ESO to regulate the robustness. This observer can be utilized to estimate the disturbances with high frequency. Reference [14] analyzed the problems of long convergence time, slow dynamic response, and poor anti-interference ability of the first-order ESO. They extended the back electromotive force of the permanent magnet synchronous motor(PMSM) to a new state and designed a second-order ESO, which improved the observation accuracy and anti-interference ability and achieved ESO control of a sensorless PMSM. In [15], Professor Zhang Yongchang and colleagues obtained the grid-side voltage reference value through the network-measured current reference value and ESO, and used it for power transistor drive. Although progresses are made in the above researches on sensorless observation and ESO estimation, they mainly focus on the motor or grid side, where the DC bus voltage estimation on the rectification side is still difficult to achieve, and few scholars have combined ESO with dynamic and static tracking. Thus, such combination is the key research topic of this paper.

On the other hand, considering the impact of voltage estimation on the overall system performance, higher requirements are proposed for the design of the internal and external loop control of the sensorless system. Existing rectifier control methods mostly use MPC, PI control, and their improved methods when operating with a sensor [17]. Reference [18] proposed an adaptive sliding mode reaching law based on exponential function for PMSM speed drive system, but the system jitter lasted a little longer. Reference [19] proposed a bi-sliding mode PI control (bi-SMPIC) of the dc-link voltage of a three-phase three-wire shunt active power filter (APF). One SMPIC can make the speed of the state variables reaching the sliding surface zero. The other SMPIC can render the state variables asymptotically stable at the origin of the sliding surface. Some scholars have used fuzzy control strategy to improve the robustness and anti-load disturbance performance of the control system [20], [21]. However, when the above research results are applied to sensorless operation, on the one hand, due to the inherent lag and errors of the observer, the dynamic tracking accuracy of the observer is affected; on the other hand, the controller parameters are designed based on steady-state conditions, and the control effect is inevitably poor during the dynamic operation of the observer switching and step changes. Therefore, it is necessary to use control methods that are compatible with the observer to ensure the overall dynamic performance of the system even under sensorless conditions.

Based on the above analysis, this paper proposes a sensorless PWM rectifier self-disturbance power prediction control strategy based on optimized ESO. Specifically, a mathematical model of the PWM rectifier is built, and the active disturbance rejection control (ADRC) and model predictive direct power control(MPDPC) in the voltage inner and outer loops are combined. The purpose of the ADRC-MPDPC is to shorten the adjustment time and reduce the steady-state voltage estimated error. Moreover, in order to find an alternative method to address the voltage sensor damage, a fault-tolerant control method is proposed. We introduced an error differential term into ESO to construct an optimized ESO, which

replaces the voltage sensor to observe the bus voltage when the sensors fail. Finally, through simulation and experimental results on the MATLAB/Simulink and rectifier-inverter test platform, the effectiveness of the above proposal is verified.

The remaining structure of this article is organized as follows: in chapter II, the mathematical model of PWM rectifier and MPDPC control are described; in chapter III: the models of optimized ESO and ADRC-MPDPC are constructed, and then we introduce the proposed fault diagnosis strategy; the results of simulations and experiments are presented in chapter IV; the conclusion is discussed in chapter V.

## II. MATHEMATICAL MODEL OF PWM RECTIFIER AND MPDPC CONTROL

The typical main circuit topology of a three-phase PWM rectifier is shown in Fig.1. The equivalent circuit equation of the three-phase voltage-type PWM rectifier can be obtained by KVL law [22]:

$$L_s \frac{di_s}{dt} = u - u_g - R_s i_s \tag{1}$$

where $u$ is the grid electromotive force vector, $i_s$ is the rectifier grid-side current vector, $u_g$ is the rectifier input voltage vector, $L_s$ is the inductance value of the grid-side filter inductance, and $R_s$ is the equivalent resistance of the grid-side inductance and the equivalent resistance of the switching tube.

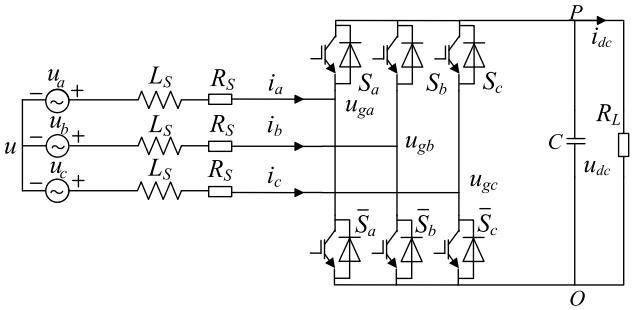


**FIGURE 1.** Main circuit topology of three-phase PWM rectifier.

The active power $p$ and reactive power $q$ of the three-phase rectifier under direct power control strategy can be expressed as [23]:

$$\begin{cases} p = u_d i_d + u_q i_q \\ q = u_d i_q - u_q i_d \end{cases} \tag{2}$$

where $u_d$, $u_q$, $i_d$, and $i_q$ are the grid-side phase voltage and input current in the $dq$ coordinate system.

Using the first-order Euler method for equation (1), the current prediction at time $k+1$ can be obtained as:

$$i_s(k+1) = \left(1 - \frac{R_s T_s}{L_s}\right) i_s(k) + \frac{T_s}{L_s}\left[u(k+1) - u_g(k)\right] \tag{3}$$

where $u(k+1) = u(k)e^{j\omega T_s}$, $\omega$ is the grid voltage angular frequency, and $T_s$ is the sampling period. If $T_s$ is small enough to be ignored, then $u(k+1) \approx u(k)$.

According to equation (2), the instantaneous power at $k+1$ time can be obtained as:

$$\begin{cases} p(k+1) = \mathrm{Re}\left\{u(k+1)\overline{i_g}(k+1)\right\} \\ q(k+1) = \mathrm{Im}\left\{u(k+1)\overline{i_g}(k+1)\right\} \end{cases} \tag{4}$$

The power controller must obtain the minimum power error with the fastest dynamic response. Considering the variance between the reference power and the predicted power, the cost function is

$$g = \left[p_{ref} - p(k+1)\right]^2 + \left[q_{ref} - q(k+1)\right]^2 \tag{5}$$

where g can evaluate the accuracy of power predication, and the smaller the value, the higher the prediction accuracy.

Traditional double-closed-loop DPC control consists of a voltage and current double-closed-loop control systems. In order to further reduce the error and achieve fast dynamic tracking of the power loop, an MPDPC scheme is used. The external loop adopts a PI controller to obtain the input reference current, and then calculates the active power reference value. The power prediction control scheme is shown in Fig.2.

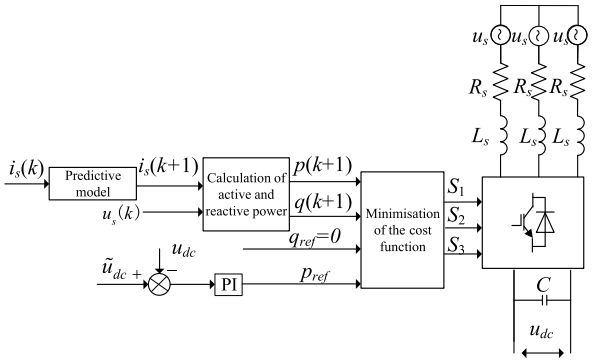


**FIGURE 2.** MPDPC control scheme based on PI controller.

## III. MODEL PREDICTIVE CONTROL OF PWM RECTIFIER BASED ON OPTIMIZED ESO BUS VOLTAGE OBSERVER

The dynamic and static response performance of the DC-side voltage external loop is crucial for the overall control of the rectifier. In the model predictive direct power control strategy, the set value of active power is calculated based on the set value of bus voltage combined with PI control. Traditional PI control parameters are designed when the system operates at unity power factor and under stable conditions. Therefore, the coordination effect under dynamic conditions still needs to be improved, and the voltage value is obtained from sensors. Once the bus voltage sensor fails, if there is no observed value in the fault-tolerant state for compensation, it will directly affect the stable operation of the system. Considering the anti-interference of ADRC itself and the good dynamic tracking performance of ESO, this paper optimizes and improves

the DC side, and proposes a comprehensive control scheme for the rectifier in combination with MPDPC.

### A. ESO BUS VOLTAGE OBSERVER DESIGN

According to the topology structure of Fig.1 and Kirchhoff's law, we can obtain:

$$\begin{cases} L_s\dfrac{di_a}{dt} + R_s i_a = u_a - (u_{dc}S_a + u_{NO}) \\ L_s\dfrac{di_b}{dt} + R_s i_b = u_b - (u_{dc}S_b + u_{NO}) \\ L_s\dfrac{di_c}{dt} + R_s i_c = u_c - (u_{dc}S_c + u_{NO}) \end{cases} \tag{6}$$

where $u_{NO} = -\frac{u_O}{3}\sum_{j=a,b,c} S_j$, $S_a$, $S_b$ and $S_c$ are the switching functions of the rectifier, they can convert AC into DC by multiplication operation with AC. Transforming equation (6) into $dq$ coordinates, we can derive the corresponding differential equation under these rotating coordinates:

$$\begin{cases} \dfrac{di_d}{dt} = -\dfrac{R_s}{L_s}i_d + \omega i_q + u_d - S_d u_{dc} \\ \dfrac{di_q}{dt} = -\omega i_d - \dfrac{R_s}{L_s}i_q + u_q - S_q u_{dc} \end{cases} \tag{7}$$

where $\omega$ is the fundamental frequency of the grid, and $S_d$, $S_q$ are the switching functions of the rectifier under $dq$ coordinates. Taking one axis as an example, the state equation of the system can be expressed as:

$$\begin{cases} \dfrac{di_d}{dt} = f + b_0 u_{dc} \\ y = i_d \end{cases} \tag{8}$$

where $f$ is the disturbance term, and $b_0$ is the controller gain. The bus voltage ESO is designed as [24]:

$$\begin{cases} e = z_1 - y \\ \dot{z}_1 = z_2 - b_1 e + b_0 u_{dc} \\ \dot{z}_2 = -b_2 e \end{cases} \tag{9}$$

where $b_1$ and $b_2$ are the observer gains.

### B. OPTIMIZED ESO BUS VOLTAGE OBSERVER DESIGN

To further suppress dynamic bus voltage fluctuations and realize real-time and dynamic accurate estimation of the DC bus voltage under dynamic loading, an error differential term is introduced to optimize the linear extended observer.

From equation (9), we can get:

$$\begin{cases} z_1 = y + e_1 \\ z_2 = f + \dot{e}_1 + b_1 e_1 \end{cases} \tag{10}$$

The error $\dot{e}_1 + b_1 e_1$ between $z_2$ and $f$ is used as feedback to correct to accelerate the convergence speed of ESO. The improved ESO is obtained as follows:

$$\begin{cases} e_1 = z_1 - y \\ \dot{z}_1 = z_2 - b_1 e_1 + b_0 u_1 \\ \dot{z}_2 = -b_2(\dot{e}_1 + b_1 e_1) \end{cases} \tag{11}$$

According to the above analysis, we can construct an optimized ESO bus voltage observer. To prove the stability of the optimized ESO, let $e_2 = z_2 - x_2$, according to equations (10) and (11), we can obtain:

$$\begin{cases} \dot{e}_1 = e_2 - b_1 e \\ \dot{e}_2 = -b_2 e_2 - \dot{f} \end{cases} \tag{12}$$

Let $Y_1 = e_1$, $Y_2 = e_2 - b_1 e_1$, we can get the equation of the ESO error system:

$$\begin{cases} \dot{Y}_1 = Y_2 \\ \dot{Y}_2 = -(b_1 + b_2)Y_2 - b_1 b_2 Y_1 - \dot{f} \end{cases} \tag{13}$$

The characteristic equation of the ESO error system is

$$s^2 + (b_1 + b_2)s + b_1 b_2 = 0 \tag{14}$$

According to the Gurevich theorem, the necessary and sufficient condition for the stability of a second-order system is $b_1 + b_2 > 0$ and $b_1 b_2 > 0$. Because the observer bandwidth $\omega_0$ is greater than 0, the system is stable. Therefore, the trivial solution ($e_1 = 0$, $e_2 = 0$) of the second-order constant coefficient differential equation shown in equation (14) is globally asymptotically stable.

When considering disturbance $f$, there is a steady-state error in the system. Let $|f| \le w_0$, $w_0 = const > 0$. When the system reaches steady state, we can obtain:

$$\begin{cases} \dot{Y}_1 = Y_2 = 0 \\ \dot{Y}_2 = 0 \end{cases} \tag{15}$$

The steady-state error can be calculated as:

$$\begin{cases} |e_1| \le \dfrac{w_0}{b_2} \\ |e_2| \le \dfrac{b_1 w_0}{b_2} \end{cases} \tag{16}$$

Therefore, under the stability condition of equation (14), the optimized ESO can achieve a smaller observation error with larger values of $b_1$ and $b_2$, where $b_2$ should be much larger than $b_1$. Based on experimental experience and multiple simulations, we assigned the value of 100 to $b_1$ and value 2500 to $b_2$.

### C. ADRC CONTROLLER DESIGN FOR VOLTAGE OUTER LOOP

Ignoring line and switching losses, according to the law of energy conservation, the DC-side power of the system is equal to the grid-side power, namely:

$$\begin{cases} P_{dc} = P_{ac} \\ P_{dc} = C\tilde{u}_{dc}\dfrac{d\tilde{u}_{dc}}{dt} + \dfrac{\tilde{u}_{dc}^2}{R_s} \\ P_{ac} = \dfrac{3}{2}u_d i_d + \dfrac{3}{2}u_q i_q \end{cases} \tag{17}$$

$u_{dc}$ is the reference value of the DC bus voltage, $C$ is the capacitance in DC-side. According to equation (17), when the

system operates at unity power factor, we have:

$$\frac{d\tilde{u}^{dc}}{2} = \frac{2\tilde{u}_{dc}^2}{R_s C} + \frac{3u_d i_d}{C} \tag{18}$$

Let $x_1 = \tilde{u}_{dc}^2$, $x_2 = -\frac{2\tilde{u}_{dc}^2}{R_s C}$, $\beta_0 = \frac{3u_d}{C}$, $u = i_d$($d$ is the differential of $x_2$, $u$ refers to the input of controller), the self-disturbance controller of the system is

$$\begin{cases} \dot{x}_1 = x_2 + \beta_0 u \\ y = x_1 \end{cases} \tag{19}$$

Fig.3 shows the ADRC structure diagram of the PWM rectifier bus voltage regulator. The self-disturbance controller is used to replace the cascaded voltage external loop and power loop controllers. It consists of a nonlinear tracking differentiator (TD), a disturbance extended state observer ($ESO_2$), a voltage extended state observer ($ESO_1$), and a nonlinear combiner (NLS). TD achieves fast tracking of the input signal, ESO estimates system disturbance and DC bus voltage separately, while NLS compensates for the disturbance.

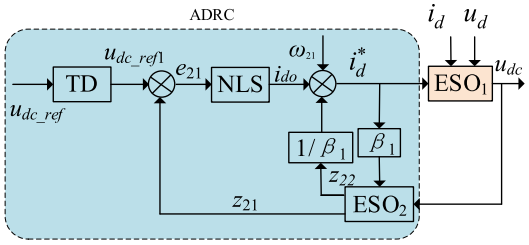


**FIGURE 3.** ADRC structure block diagram.

### 1) TRACKING DIFFERENTIATOR DESIGN

To achieve limitations on the rate of change, an appropriate transition process is arranged for a given bus voltage command $u_{dc\_ref}$ as follows:

$$\begin{cases} \dot{u}_{dc\_ref1} = u_{dc\_ref2} \\ \dot{u}_{dc\_ref2} = -1.73 \times r_1 \times u_{dc\_ref2} \\ \quad -r_1^2 \times (u_{dc\_ref1} - u_{dc\_ref}) \end{cases} \tag{20}$$

Here, $r_1$ is the adjustable parameter for TD. A larger $r_1$ results in a faster tracking speed, but if $r_1$ is too large, it will cause overshoot. The transition process curve can be selected based on the characteristics of the PWM rectifier, and the appropriate adjustable parameter can then be chosen according to the curve, where $u_{dc\_ref1}$ is the arranged transition process, and $u_{dc\_ref2}$ is the differential signal obtained by the tracking differentiator.

### 2) EXTENDED STATE OBSERVER DESIGN

To estimate the uncertain factors as an extended state and transform the nonlinear control system into a linear control system, an optimized ESO is used:

$$\begin{cases} e_{21} = z_{21} - x_1 \\ \dot{z}_{21} = z_{22} - \beta_1 e_{21} + \beta_0 u \\ \dot{z}_{22} = -\beta_2(\dot{e}_{21} + \beta_1 e_{21}) \end{cases} \tag{21}$$

Here, $z_{21}$ and $z_{22}$ are the state estimates of voltage and disturbance, and $\beta_1$ and $\beta_2$ are observer gains. By bandwidth parameterization, all the poles of the three observers are configured to the corresponding locations -$\omega_1$, resulting in the following expression.

$$[\beta_1 \ \beta_2 \ ]^T = [2 - \omega_1 \ \omega_1^2 \ ]^T \tag{22}$$

### 3) CONTROL LAW DESIGN

The control law is designed by linearly combining the error between the transition process and state estimation and compensating for the disturbance estimation. The expression is as follows:

$$\begin{cases} i_{d0} = k_1(i_{dc\_ref1} - z_{21}) \\ i_d^* = i_{d0} - \dfrac{z_{22}}{\beta_1} \end{cases} \tag{23}$$

Here, $i_d^*$ is the estimated value of $i_d$, it can serve as a feedback to $ESO_1$ and $ESO_2$. $k_1$ is the adjustable parameter for NLS and has proportional and differential effects. Therefore, the adjustment method of $k_1$ can refer to PID. Increasing $k_1$ can speed up the response of the system, but it is worth noting that an excessive value of $k_1$ will cause the overshoot during the adjustment process. Experiment results indicated that the optimal interval for the value of $k_1$ is 5-14. We chose a value of 7 for it. Moreover, to ensure the model stability and robustness, the model weight λ is 0.2.

### 4) FAULT DIAGNOSIS STRATEGY

In voltage sensorless control, online fault diagnosis can detect sensor faults and switch the system to observer operation mode to ensure safe operation and avoid major accidents. The residual between the bus voltage observation value and the measured value is used as the basis for fault detection, and its calculation method is as follows [25]:

$$u_{re} = \frac{|u_{dc} - u_{dc}^*|}{\tilde{u}_{dc}} \tag{24}$$

Here, $u_{re}$ is the residual. When the voltage sensor is functioning normally, the residual is small. When the voltage sensor has a fault, the residual will exhibit a mutation. This feature can be used as a criterion for fault detection. After the system starts for 1 s, the three observation errors $u_{dc\_error1}$ – $u_{dc\_error3}$ are recorded in descending order and their arithmetic mean $u_{th}$ is calculated as the fault judgment threshold. The threshold is updated by rolling the error values under non-fault conditions. At 2 s, the observation voltage $u_{dc}^*$ is compared with the set value $u_{dc}$, and if it is greater than or equal to 20%, it is determined that the voltage sensor has a startup fault. If it is less than 20%, the operation fault judgment is initiated. To avoid misjudgment, a threefold

margin is established as the judgment standard. Specifically, if the observation error is greater than three times the $u_{th}$ for five consecutive sampling periods, it is determined that the voltage sensor has a fault, and the system is switched to the ESO observer mode for continued operation.

#### 5) INTEGRATED CONTROL STRATEGY

Based on power prediction control, an optimized ESO bus voltage observer is employed to achieve model predictive power control without voltage sensors, and a self-disturbance rejection control strategy is adopted to further enhance the system's dynamic response. The ADRC replaces the PI controller in MPDPC control scheme. The module of fault diagnosis is used to calculate the $u_{re}$ and switch the system to observer operation mode. The inner loop is composed of current prediction, instantaneous power calculation and MPDPC. The outer loop is composed of ADRC, optimized ESO and, fault diagnosis. This paper presents the integrated control structure diagram of the optimized ESO voltage-sensorless ADRC-MPDPC, as shown in Fig.4.

During the process of parameter adjustment, we utilized the principle of separability to adjust the parameters and variables of TD, ESO and NLS. Then we integrated the three parts for performance adjustment.

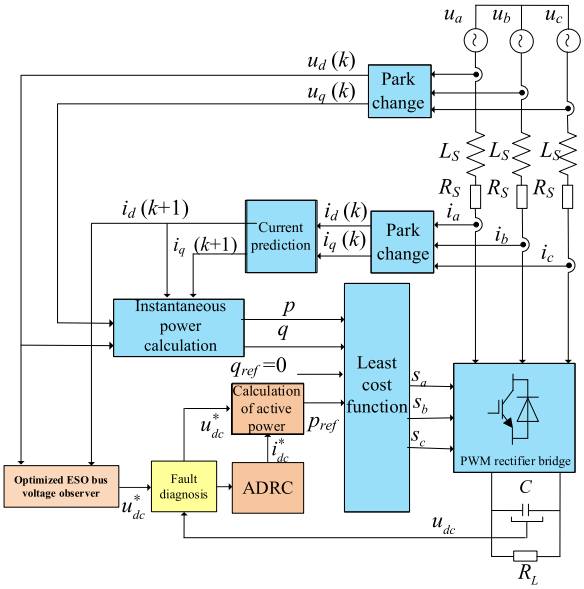


**FIGURE 4.** Integrated control structure diagram.

## IV. SIMULATION AND EXPERIMENT

### A. SYSTEM SIMULATION

To verify the effectiveness of the ADRC-MPDPC control strategy based on the bus voltage ESO observer, a simulation model was established in MATLAB/Simulink to compare and verify the bus voltage observation effect and the three control methods of DPC, MPDPC, and ADRC-MPDPC without voltage sensors. The simulation parameters and control parameters of the model are shown in Table.1.

When using DPC from start-up to steady state, simulation diagrams of grid-side current, active power and reactive power, and DC bus voltage are shown in Figs.5(a), 5(b), and 5(c), respectively. From Fig.5(a), it can be observed that the convergence time of the grid-side current to steady-state is 0.05 s, and the current fluctuates due to harmonic interference, presenting a nonstandard sine wave. In Fig.5(b), due to the use of logical switch tables, there are some mutations in active power adjustment, and the convergence time of active power is about 0.03 s. From Fig.5(c), it can be observed that the DC bus voltage fluctuates greatly during start-up, with a maximum fluctuation of 40 V, and the rise time of the bus voltage is slow, taking 0.025 s, and the pulsation in steady state is around 4 V.

Fig.6 shows the start-up and steady-state simulation waveforms using MPDPC, corresponding to the three diagrams in Fig.5. The current convergence time is reduced to 0.022 s, and the waveform presents a standard sine wave, but the convergence time of active power is extended to 0.04 s. Although there is still a large voltage fluctuation during start-up, the maximum fluctuation is reduced to 30 V, and the rise time is also slow, taking 0.02 s. When reaching steady state, the pulsation is around 3.8 V.

Fig.7 shows the start-up and steady-state simulation waveforms using ADRC-MPDPC. From the figure, we can obtain that the convergence speed of active power is faster than DPC and MPDPC, and the convergence time is about 0.022 s. The voltage overshoot during start-up disappears. The rise time is reduced to 0.0096 s, and the stable pulsation is around 1.8 V.

In the ESO observer, the accuracy of the grid-side current (input variable) affects the voltage observation effect. Figs.8(a), 8(b), and 8(c) show the harmonic analysis of the grid-side current for the three strategies mentioned above. It can be observed that the harmonic distortion is the smallest under the ADRC-MPDPC strategy, which also indicates that the voltage observation performance is superior with this strategy.

Fig.9 shows the comparison between the actual and estimated DC bus voltages under the three strategies, along with the observation error. Figs.9(a), (b), and (c) present the simulation waveforms under DPC, MPDPC, and ADRC-MPDPC, respectively, and Fig.9(d) shows the comparison of observation errors under the three strategies. We added filters to the three models. From the figures, it is evident that the maximum observed voltage error is about 4 V in Figs.9(a) and 9(b), and the observed waveform is not close to the true waveform. When the disturbance is further mitigated by adding ADRC-MPDPC, the fluctuation is substantially minimized, and the estimated voltage curve closely matches the actual DC bus voltage. The simulation results demonstrate that the combination of ADRC-MPDPC control strategy and ESO yields improved observation accuracy.

Figs.10-12 are simulation comparison diagrams of bus voltage, grid-side three-phase current, and power control

**TABLE 1. Parameter table.**

| Model Parameters | | Control Parameters | | | |
|---|---|---|---|---|---|
| Parameters | Value | ESO Observer | | MPDPC | |
| Grid power phase voltage $u_{abc}$ | 220 V | Gain coefficient $b_1$ | 100 | Proportional gain $K_p$ | 0.25 |
| Grid voltage frequency $f$ | 50 HZ | Gain coefficient $b_2$ | 2500 | Integral gain $K$ | 5 |
| DC bus voltage $u_{dc}$ | 520 V | | | Weight $\lambda$ | 0.2 |
| Grid-side resistance $R_g$ | 15 mΩ | DPC | | ADRC-MPDPC | |
| DC side filter capacitor $C$ | 2200 μF | Proportional gain $K_p$ | 0.25 | TD adjustment $r_1$ | 633 |
| Load resistance $R_{dc}$ | 30 Ω | Integral gain $K_i$ | 5 | Gain coefficient $\beta_1$ | 300 |
| Sampling period $Ts$ | 4e-5 s | Active lag width $H_p$ | 200 W | Gain coefficient $\beta_2$ | 2250 |
| Grid-side input inductance $L_g$ | 5.5 mH | Reactive lag width $H_q$ | 100 Var | NLS adjustment $k_1$ | 7 |
| | | | | Weight $\lambda$ | 0.2 |

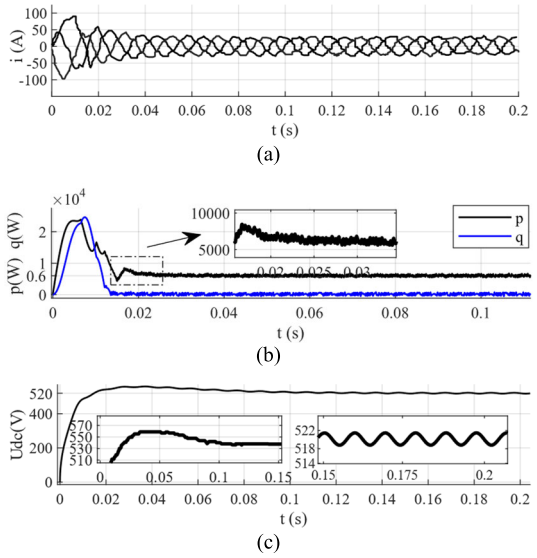


**FIGURE 5. Start up and steady state simulation diagram using DPC, (a) grid-side current, (b) active power and reactive power, (c) DC bus voltage.**

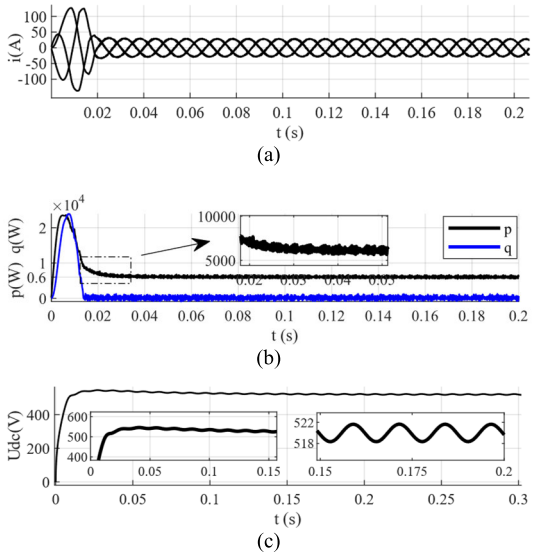


**FIGURE 6. Start up and steady state simulation diagram using MPDPC, (a) grid-side current, (b) active power and reactive power, (c) DC bus voltage.**

under dynamic step. At 1s, the bus voltage reference steps from 520 V to 400 V, and at 1.3 s, a 50 Ω load is connected in parallel to reduce the load from 100 Ω to 50 Ω. According to the Fig.10, the fluctuation of bus voltage using ADRC-MPDPC is minimal, demonstrating superior stability compared to DPC and MPDPC. Table 2 summarizes the results of performance comparison among three strategies. Compared with DPC and MPDPC, the ADRC-MPDPC reduces the estimate voltage error by approximately 2 V. And the system response time is also decreased by this method. These results confirm that the ADRC-MPDPC method provides the best accuracy and stability.

Under the proposed strategy, Figs.11 and 12 show the AC current simulation diagrams, and active and reactive power simulation diagrams using voltage sensor and ESO observers, respectively.

It can be observed that when the control parameters are changed, the steady-state control performance of the two observation methods are basically the same, indicating that the ESO voltage observer ensures stable operation of the system.

Fig.13 illustrates the simulation process of automatic switching to observer mode in case of a simulated voltage sensor fault. Fig.13(a) shows the actual bus voltage before

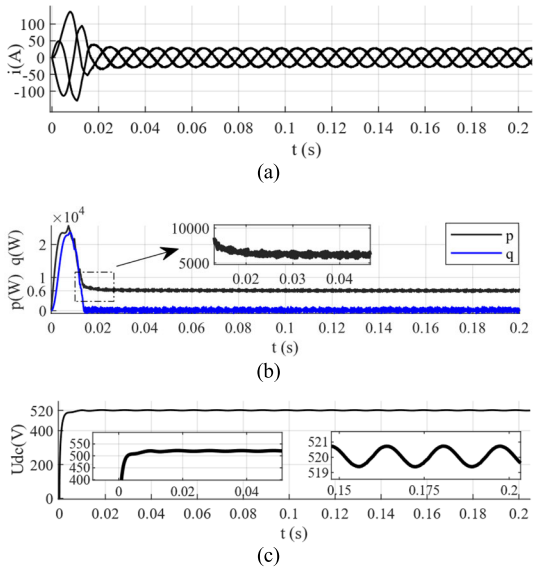


**FIGURE 7.** Start up and steady state simulation diagram using ADRC-MPDPC, (a) grid-side current, (b) active power and reactive power, (c) DC bus voltage.

**TABLE 2.** Simulation data comparison for different strategies.

| | DPC | MPDPC | ADRC-MPDPC |
|---|---|---|---|
| Udc Max estimated error | 4 V | 3.8 V | 1.8 V |
| Udc Fluctuation (Bus voltage step) | 21 V | 15 V | 0 V |
| Udc Fluctuation (Load mutation) | 9 V | 7 V | 1 V |
| Convergence time of *i* (Start up) | 0.05 s | 0.022 s | 0.018 s |
| Convergence time of *PQ* (Start up) | 0.03 s | 0.04 s | 0.022 s |
| Udc Rise time | 0.025 s | 0.02 s | 0.0096 s |
| Udc Adjustment time | 0.08 s | 0.065 s | 0.016 s |
| Total harmonic distortion | 13.22 % | 8.34 % | 3.80 % |

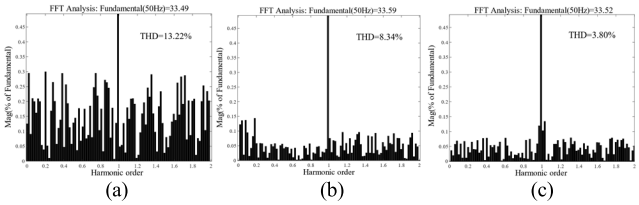


**FIGURE 8.** AC current harmonic comparison diagram.

and after the fault. In Fig.13(b), th is the fault threshold, calculated from the observation error. At 2.5 s, the voltage sensor output is stepped to 600 V, causing the observation error to increase rapidly and exceed the fault threshold for five consecutive sampling periods. The system switches to ESO voltage observer mode automatically and gradually returns to stability, with no change in the DC side voltage.

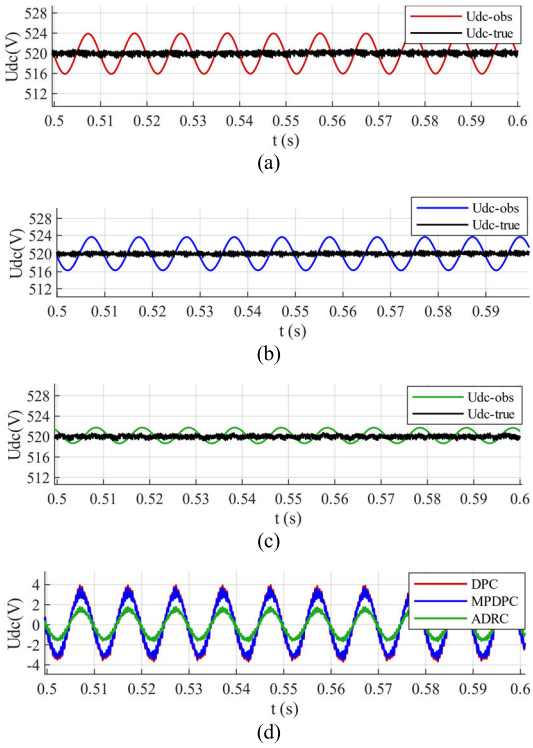


**FIGURE 9.** Comparison diagram of voltage actual value, estimated value and error in steady state, (a) DPC, (b) MPDPC, (c) ADRC-MPDPC, (d) Comparison of observation errors under the three strategies.

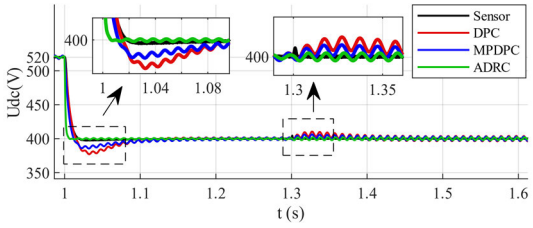


**FIGURE 10.** Voltage simulation diagram of set value of bus voltage and load step response.

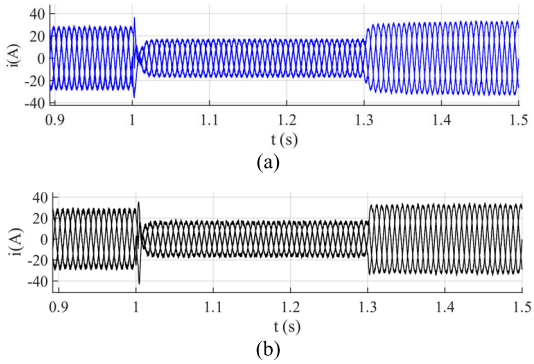


**FIGURE 11.** AC current simulation diagram of set value of bus voltage and load step response, (a) voltage sensors, (b) ESO voltage observer.

The results of robustness validation are presented in Fig.14. Under the real values of $R_g = 15$ mΩ and $L_g = 5.5$ mH,

the first row in Figs.14(a) and (b) consist of three sections: $L_g = 5.5$ mH, $L_g = 8.5$ mH, and $L_g = 11.5$ mH, respectively; the second row in Figs.14(a) and (b) also consist of three sections: $R_g = 15$ mΩ, $R_g = 0.15$ Ω, and $R_g = 1.5$ Ω, respectively. Fig.14(a) shows that the bus voltage waveforms hardly change, and the maximum fluctuation is about 1.8 V all the time. The active power is always between 5.5 kw and 6 kw. These results demonstrate that the proposal has excellent robustness when the system parameters change.

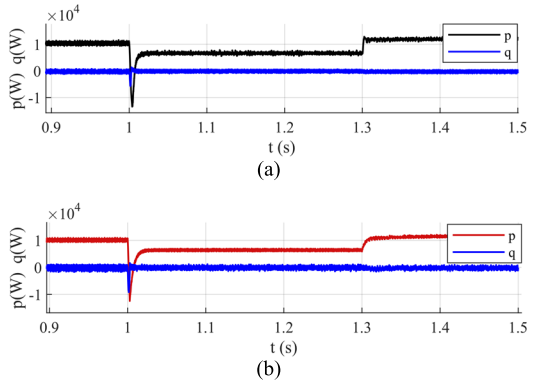


**FIGURE 12.** Active and reactive power simulation diagram of set value of bus voltage and load step response, (a) voltage sensors, (b) ESO voltage observer.

The simulation results show that the rectifier controlled by the observer maintains stable control when the system parameters change. The main parameters in the ADRC-MPDPC control can promptly return to a stable state. Compared with direct control using voltage sensors, although the adjustment time is slightly delayed, the steady-state value is basically the same. This approach enables both dynamic and steady-state control without the need for bus voltage sensors, effectively preventing major operational failures.

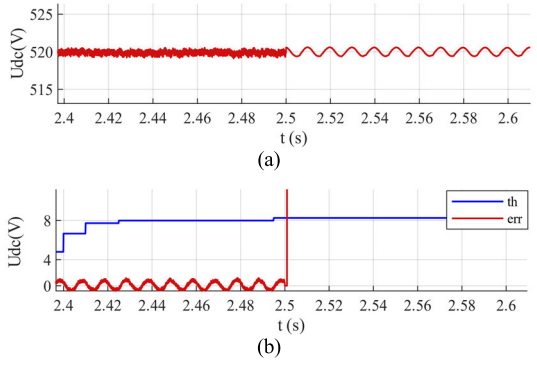


**FIGURE 13.** Simulation diagram of sensor fault tolerant control, (a) bus voltage before and after the sensor fault, (b) fault threshold and error.

### B. EXPERIMENTAL VERIFICATION

To validate the actual performanceof the control strategies proposed in this article, experiments were conducted on a self-developed experimental platform, as shown in Fig.15.

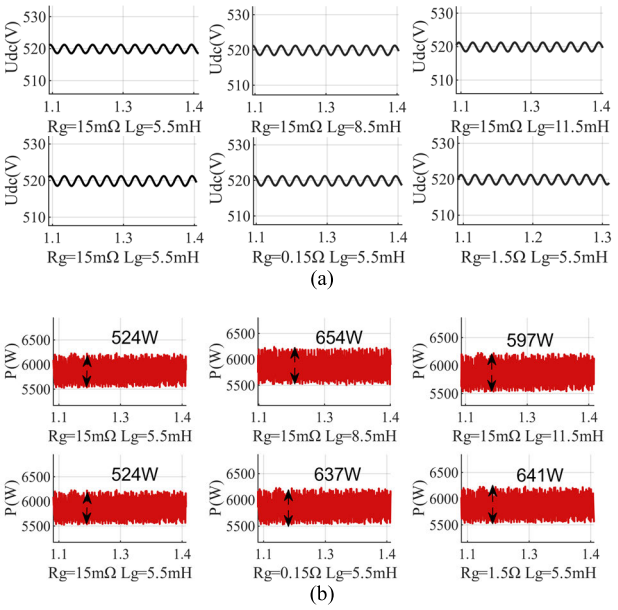


**FIGURE 14.** Simulation diagrams of robustness validation, (a) bus voltage, (b) active power.

The system's main circuit features a voltage-type AC-DC-AC topology. The control module is composed of the rectifier side and the inverter side, and the rectifier control uses PWM pulse rectification to achieve four-quadrant rectification. High-performance IGBT components are employed for the rectifier, and the strategy of model predictive direct torque control(MPDTC) controls the inverter side. The system's load consists of a motor support structure, which includes an asynchronous motor (model 1LA7096-4A10-Z) and a permanent magnet synchronous motor (model 1FT6). The control system is implemented on a high-speed DSP (TMS320F28335), which handles the control algorithm and PWM pulse calculation, while a field programmable gate array (FPGA) is used for distributed data acquisition and hardware protection. The main parameters of the experimental device are the same as the simulation, and the main parameters of motor are shown in Table 3.

**TABLE 3.** System parameters.

| Main Parameters of Motor | | $R_r$/Rotor resistance | 1.85681 Ω |
|---|---|---|---|
| $P_n$/Rated Power | 2.2 kW | $L_r$/Rotor inductance | 12.65 mH |
| $V_n$/Rated bus voltage | 400 V | $L_m$/Mutual inductance | 0.3 H |
| $R_s$/Stator resistance | 3.1 Ω | $p$/Polar number | 2 |
| $L_s$/Stator inductance | 12.65 mH | $J$/Inertia | 0.1 kg·m² |
| $f$/Rectifier switch frequency | 25 kHZ | $T_n$/Rated torque | 28 N·m |
| $K_i$/Integral Gain | 1.5 | $h_p$/Error feedback factor | 0.8 |

Fig.16 shows the steady-state waveform diagrams of the DC bus voltage $u_{dc}$ observed by voltage sensor and ESO and observation error. It can be observed that the actual voltage fluctuation using ADRC control is within 1 V, and the

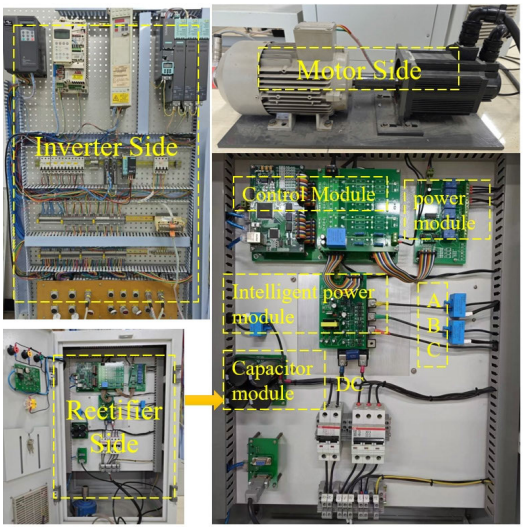


**FIGURE 15.** Experimental device diagram.

pulsation range of the observed voltage value is within 2 V, with an observation error remaining within 2 V. The ESO can effectively measure the bus voltage.

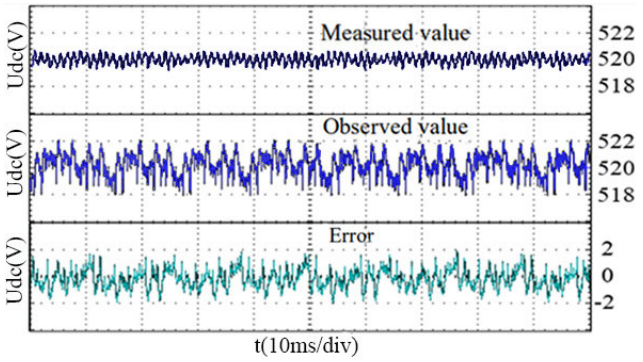


**FIGURE 16.** Experimental diagram of DC bus voltage in steady state.

To verify the dynamic performance of the rectifier without using a bus voltage sensor, a comparative experiment was conducted under identical parameter change, employing both a voltage sensor and an ESO voltage observer. Fig.17 and 18 show the changes in bus voltage, as well as the active and reactive power, when the voltage setpoint is stepped down from 520 V to 400 V. At the moment of voltage step, the observed voltage fluctuation is 5 V, and the adjustment time for the sensorless control method is about 75 ms.

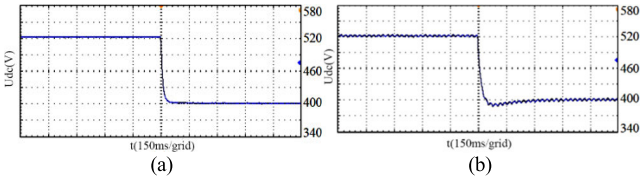


**FIGURE 17.** Voltage experimental diagram of set value of bus voltage step response, (a) voltage sensor, (b) ESO voltage observer.

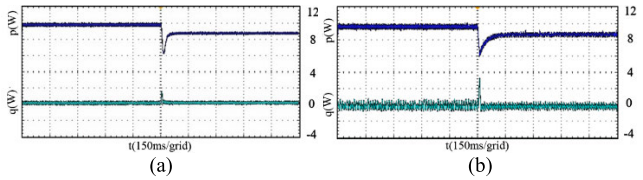


**FIGURE 18.** Power experimental diagram of set value of bus voltage step response, (a) voltage sensor, (b) ESO voltage observer.

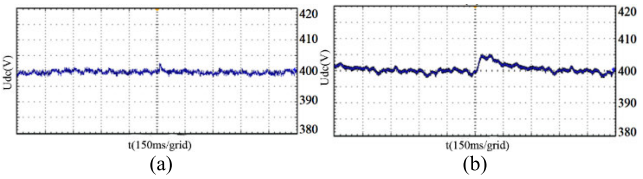


**FIGURE 19.** Voltage experimental diagram of torque step response, (a) voltage sensor, (b) ESO voltage observer.

Fig.19 and 20 show the changes in bus voltage, as well as the active and reactive power, when the motor torque is increased from 0 N·m to 10 N·m. It can be observed that the overshoot of the bus voltage increases by 3 V, with a maximum fluctuation of 1.25%, which is well below the national standard requirement of 7%. Additionally, the adjustment time for the sensorless control method is about 100 ms.

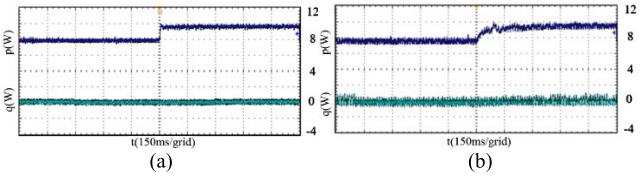


**FIGURE 20.** Power experimental diagram of torque step response, (a) voltage sensor, (b) ESO voltage observer.

Fig.21 shows the experimental diagram of fault-tolerant control in case of a simulated gain fault of the voltage sensor. Fig.21(a) illustrates the actual measured bus voltage before and after the fault, while Fig.21(b) depicts the observation error of the observer and the fault detection threshold. Upon activation of fault-tolerant control, the detection threshold adjusts according to the observation error. When the voltage sensor fails, the observation error rapidly exceeds the threshold, and the controller automatically switches to ESO mode operation. The bus voltage fluctuates within 2 V, proving the effectiveness of the fault-tolerant algorithm.

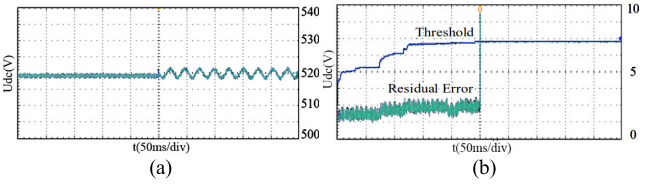


**FIGURE 21.** Experimental diagram of sensor fault tolerant control, (a) bus voltage before and after the sensor fault, (b) fault threshold and error.

In summary, the experiments have confirmed that the ESO can accurately estimate the DC bus voltage in the ADRC-MPDPC control method. The fault-tolerant control algorithm enables the system to promptly switch to ESO observer mode when a sensor fault is detected, and the rectifier can rapidly recover stable operation under external disturbances that cause parameter perturbations.

## V. CONCLUSION

This article presents an active disturbance rejection power predictive control method for PWM rectifiers, based on an optimized ESO observer, to address the issue of DC bus voltage sensor failure. An ESO with an error differential term was constructed to estimate the bus voltage. In the event of sensor failure, the dynamic tracking and control of the bus voltage under the sensorless condition are achieved by integrating inner loop model predictive control, external loop self-disturbance control, and ESO observer. Simulation and experimental results of the proposed integrated control system show that:

1) The observation error of the proposed observer is within 2 V in steady state, and 5 V when the bus voltage undergoes a step change. When the motor torque undergoes a step change, the adjustment time of the sensorless control method is only 100 ms, with a maximum voltage fluctuation of 1.25%, well below the national standard requirements. These performances denote that the proposed observation method has excellent observation ability and can replace voltage sensor in the event of failure.
2) Under the ESO operation mode, compared with traditional PI control, the combination of ADRC and ESO can make the system converge to a stable state more rapidly during dynamic response, and the maximum steady-state error is reduced by about 2 V. Therefore, the ADRC-MPDPC strategy provides the system with enhanced stability and improved response performance.
3) By detecting abnormal fluctuations in estimation errors, the failure of the bus voltage sensor can be diagnosed, allowing the system to switch to observer operation promptly and restore stable performance. This provides an effective fault-tolerant control method to address voltage sensor malfunctions.

The performance of the observation system can be further improved by eliminating the adjustment time. Additionally, further optimization of the control scheme could reduce the observation error. These issues will be a key focus of future research.

## REFERENCES


[1] S. Kwak and H. A. Toliyat, "Design and rating comparisons of PWM voltage source rectifiers and active power filters for AC drives with unity power factor," *IEEE Trans. Power Electron.*, vol. 20, no. 5, pp. 1133–1142, Sep. 2005, doi: 10.1109/TPEL.2005.854055.

[2] R. Teodorescu, M. Liserre, and P. Rodriguez, *Grid Converters for Photovoltaic and Wind Power Systems*. Hoboken, NJ, USA: Wiley, 2011.

[3] B Liu, X. Y. Feng, R. Deng, W. J. Xia, and W. S. Song, "Grid voltage sensorless control strategy of single-phase PWM rectifiers with model reference adaptive system," *Proc. CSEE*, vol. 39, no. 20, pp. 6065–6074, 2019, doi: 10.13334/j.0258-8013.pcsee.182187.

[4] Z. Zhang, Z. Li, M. P. Kazmierkowski, J. Rodriguez, and R. Kennel, "Robust predictive control of three-level NPC back-to-back power converter PMSG wind turbine systems with revised predictions," *IEEE Trans. Power Electron.*, vol. 33, no. 11, pp. 9588–9598, Nov. 2018, doi: 10.1109/TPEL.2018.2796093.

[5] X. Wang, Z. Wang, Z. Xu, M. Cheng, W. Wang, and Y. Hu, "Comprehensive diagnosis and tolerance strategies for electrical faults and sensor faults in dual three-phase PMSM drives," *IEEE Trans. Power Electron.*, vol. 34, no. 7, pp. 6669–6684, Jul. 2019, doi: 10.1109/TPEL.2018.2876400.

[6] Z. Chen, C. Yang, T. Peng, H. Dan, C. Li, and W. Gui, "A cumulative canonical correlation analysis-based sensor precision degradation detection method," *IEEE Trans. Ind. Electron.*, vol. 66, no. 8, pp. 6321–6330, Aug. 2019, doi: 10.1109/TIE.2018.2873100.

[7] H. Wang, Y. Zhang, X. Xiao, X. Wang, and S. Han, "SMO-ESO-based voltage sensorless model predictive control for PWM rectifier," in *Proc. 4th Int. Conf. Smart Power Internet Energy Syst. (SPIES)*, Beijing, China, Dec. 2022, pp. 1047–1052, doi: 10.1109/SPIES55999.2022.10082473.

[8] X. Xiong, W. Yujuan, and S. Guangda, "Voltage-sensorless model predictive power control of PWM rectifier based on adaptive neural network observation," *Proc. CSEE*, vol. 41, no. 3, pp. 1135–1146, 2021, doi: 10.13334/J.0258-8013.PCSEE.200926.

[9] S.-K. Kim, S. Lim, and K.-B. Lee, "Nonlinear damping output-feedback voltage control for DC/DC converters via model-independent voltage derivative observer," *IEEE Trans. Ind. Electron.*, vol. 70, no. 8, pp. 7924–7933, Aug. 2023, doi: 10.1109/TIE.2023.3236090.

[10] P. Li, X. Tong, W. Jin, and T. Chen, "Observer based model predictive current control of distorted grid connected single phase rectifier without AC voltage sensor," *Control Eng. Pract.*, vol. 138, Sep. 2023, Art. no. 105589, doi: 10.1016/j.conengprac.2023.105589.

[11] T. Qingfang and C. Hongwei, "ESO-based model predictive torque control for PMSM drive system with single pahse current sensor," *Acta Energiae Solaris Sinica*, vol. 41, no. 9, pp. 129–138, 2020.

[12] M. Ran, J. Li, and L. Xie, "A new extended state observer for uncertain nonlinear systems," *Automatica*, vol. 131, Sep. 2021, Art. no. 109772, doi: 10.1016/j.automatica.2021.109772.

[13] S. Zhuo, S. Jin, X. Liu, H. Bai, Y. Huangfu, and F. Gao, "Robust voltage control with resonant extended state observer for hybrid fuel cell system," *IEEE Trans. Power Electron.*, vol. 39, no. 5, pp. 5462–5472, May 2024, doi: 10.1109/TPEL.2024.3367907.

[14] Z. Yang, T. Jie, S. Minglei, Z. Tao, and L. Chuang, "Research on sensorless control for PMSM system based on extended state observer," *Micromotors*, vol. 51, no. 1, pp. 44–49, 2018, doi: 10.15934/j.cnki.micromotors.2018.01.009.

[15] Y. Zhang, J. Jin, and L. Huang, "Model-free predictive current control of PMSM drives based on extended state observer using ultralocal model," *IEEE Trans. Ind. Electron.*, vol. 68, no. 2, pp. 993–1003, Feb. 2021, doi: 10.1109/TIE.2020.2970660.

[16] W. Zhankuo, Z. Yongchang, and T. Chaonan, "Improved model predictive direct power control for three-phase PWM rectifier," *Electr. Mach. Control*, vol. 24, no. 7, pp. 73–81, 2020, doi: 10.15938/j.emc.2020.07.008.

[17] W. Chengshan, L. Wei, and W. Yifeng, "DC bus voltage fluctuation classification and restraint methods review for DC microgrid," *Proc. CSEE*, vol. 37, no. 1, pp. 84–97, 2017, doi: 10.13334/j.0258-8013.pcsee.160807.

[18] Z. Zhang, X. Yang, W. Wang, K. Chen, N. C. Cheung, and J. Pan, "Enhanced sliding mode control for PMSM speed drive systems using a novel adaptive sliding mode reaching law based on exponential function," *IEEE Trans. Ind. Electron.*, vol. 71, no. 10, pp. 11978–11988, Oct. 2024, doi: 10.1109/TIE.2023.3347845.

[19] Z. Li, M. Ren, Z. Chen, G. Liu, and D. Feng, "A bi-sliding mode PI control of DC-link voltage of three-phase three-wire shunt active power filter," *IEEE J. Emerg. Sel. Topics Power Electron.*, vol. 10, no. 6, pp. 7581–7588, Dec. 2022, doi: 10.1109/JESTPE.2022.3168313.

[20] X. Liu, L. Qiu, Y. Fang, K. Wang, Y. Li, and J. Rodríguez, "A fuzzy approximation for FCS-MPC in power converters," *IEEE Trans. Power Electron.*, vol. 37, no. 8, pp. 9153–9163, Aug. 2022, doi: 10.1109/TPEL.2022.3157847.

[21] Y. Wang, Z. Wang, L. Zou, and H. Dong, "Observer-based fuzzy PID tracking control under try-once-discard communication protocol: An affine fuzzy model approach," *IEEE Trans. Fuzzy Syst.*, vol. 32, no. 4, pp. 2352–2365, Apr. 2024, doi: 10.1109/TFUZZ.2024.3350341.
[22] L. Yin, Z. Zhao, T. Lu, S. Yang, and G. Zou, "An improved DC-link voltage fast control scheme for a PWM rectifier-inverter system," *IEEE Trans. Ind. Appl.*, vol. 50, no. 1, pp. 462–473, Jan. 2014.
[23] A. Djerioui, K. Aliouane, and F. Bouchafaa, "Sliding mode direct power control strategy of a power quality based on a sliding mode observer," *Int. J. Electr. Power Energy Syst.*, vol. 56, pp. 325–331, Mar. 2014.
[24] S. E. Talole, J. P. Kolhe, and S. B. Phadke, "Extended-state-observer-based control of flexible-joint system with experimental validation," *IEEE Trans. Ind. Electron.*, vol. 57, no. 4, pp. 1411–1419, Apr. 2010, doi: 10.1109/TIE.2009.2029528.
[25] Y. Zhang and H. Yang, "Two-vector-based model predictive torque control without weighting factors for induction motor drives," *IEEE Trans. Power Electron.*, vol. 31, no. 2, pp. 1381–1390, Feb. 2016.

**XIONG XIAO** received the B.S. and Ph.D. degrees in control science and engineering from the University of Science and Technology Beijing, in 2010 and 2017, respectively.

From 2017 to 2019, he was a Postdoctoral Researcher with the University of Science and Technology Beijing, where he was an Associate Professor with the National Engineering Research Center for Advanced Rolling and Intelligent Manufacturing. His research interests include advanced control algorithms, data-driven, power electronics, and electrical transmission. He is a Reviewer of journals, such as IEEE TRANSACTIONS ON INDUSTRIAL ELECTRONICS, IEEE TRANSACTIONS ON INDUSTRY APPLICATIONS, and *Chinese Society for Electrical Engineering Journal of Power and Energy Systems*.

**JUNYU ZHAO** received the B.S. degree from the School of Automation, Beijing Information Science and Technology University, Beijing, China, in 2023. He is currently pursuing the M.S. degree in control science and engineering with the University of Science and Technology Beijing, Beijing. His research interests include industrial power electronics and electrical drives.

**XIAN SONG** was born in Shijiazhuang, China. He received the B.E. degree from China Three Gorges University, the M.E. degree from the University of Science and Technology Beijing, and the Ph.D. degree from Zhejiang University. He is currently a Postdoctoral Researcher with the Department of Applied Biology and Chemical Technology, The Hong Kong Polytechnic University. His research interests include flexible electronic design, sensing signal purification, and artificial intelligence for advanced medical applications.

**YUNTAO ZHAO** received the Ph.D. degree from Beijing University of Science and Technology, in 2010. He is currently a Professor with the School of Information Science and Engineering, Wuhan University of Science and Technology. His main research interests include 3D machine vision and robotics.

**YONGJUN ZHANG** received the Ph.D. degree in control theory and control engineering from the University of Science and Technology Beijing, Beijing, China, in 2010.

He is currently a Ph.D. Supervisor with the University of Science and Technology Beijing. His research interests include advanced automatic control algorithms and industrial applications, knowledge modeling and optimization, complex industrial process modeling and optimization, power electronics and converter technology, knowledge modeling, optimization pattern recognition, and intelligent control.

**FEI ZHANG** (Member, IEEE) received the Ph.D. degree in control theory and control engineering from the University of Science and Technology Beijing, Beijing, China, in 2007.

He is currently an Associate Professor with the Institute of Engineering Technology, University of Science and Technology Beijing. His research interests include industrial automation, data mining, intelligent diagnosis, and expert systems.